Proton Radiation Hardness of Perovskite Solar Cells Utilizing a Mesoporous Carbon Electrode

Declan Hughes,* Simone M. P. Meroni, Jérémy Barbé, Dimitrios Raptis, Harrison K. H. Lee, Keith C. Heasman, Felix Lang, Trystan M. Watson, and Wing C. Tsoi*

When designing spacefaring vehicles and orbital instrumentation, the onboard systems such as microelectronics and solar cells require shielding to protect them from degradation brought on by collisions with high-energy particles. Perovskite solar cells (PSCs) have been shown to be much more radiation stable than Si and GaAs devices, while also providing the ability to be fabricated on flexible substrates. However, even PSCs have their limits, with higher fluences being a cause of degradation. Herein, a novel solution utilizing a screen-printed, mesoporous carbon electrode to act bi-functionally as an encapsulate and the electrode is presented. It is demonstrated that the carbon electrode PSCs can withstand proton irradiation up to 1×10^{15} protons cm^{-2} at 150 KeV with negligible losses ($<0.07\%$) in power conversion efficiency. The 12 µm thick electrode acts as efficient shielding for the perovskite embedded in the mesoporous TiO_2. Through Raman and photoluminescence spectroscopy, results suggest that the structural properties of the perovskite and carbon remain intact. Simulations of the device structure show that superior radiation protection comes in conjunction with good device performance. This work highlights the potential of using a carbon electrode for future space electronics which is not limited to only solar cells.

D. Hughes, S. M. P. Meroni, J. Barbé, D. Raptis, H. K. H. Lee,
T. M. Watson, W. C. Tsoi
SPECIFIC, College of Engineering
Swansea University
Bay Campus, Fabian Way, Swansea SA1 8EN, UK
E-mail: 823426@swansea.ac.uk; W.C.tsoi@swansea.ac.uk

K. C. Heasman
Ion Beam Centre, Advanced Technology Institute
University of Surrey
Guildford, Surrey GU2 7XH, UK

F. Lang
Cavendish Laboratory, Department of Physics
University of Cambridge
Cambridge CB3 0HE, UK

1. Introduction

Since the launch of Explorer 1 and 3, which led to the discovery of the Van Allen belts in 1958, tremendous effort has been given to protect spacefaring electronic systems and astronauts from the harsh particle environments of a low Earth orbit (LEO), which lies from 160 to 1000 km, and beyond, to the likes of a geosynchronus orbit which lies at 35 786 km.[1,2] The Van Allen Belts stretch from 200 to 60 000 km above the Earth's surface, split into an inner and outer belt and contain a vast array of energetic protons and electrons. Proton energies range from 30 keV to 100 MeV and electron energies in the range of 100 keV to 5 MeV in the lower belt, with the outer belt possessing higher energy electrons (<10 MeV) and lower energy protons (<5 MeV).[3] When designing electronic systems and habitation compartments, care must be taken to mitigate the degradation caused by these particles.

It has been shown that under bombardment from electrons, protons, and neutrons, there can be dramatic consequences on microelectronic components. In semiconductors, degradation has been known to stem through ionization and lattice displacement and work related to this issue began in the late 20th century.[4–6] Electrons with energies of around 255 keV are needed to create a Frenkel pair in silicon (an interstitial and vacancy), and 8 MeV to create an agglomeration of defects (cluster). Protons and neutrons can cause the same effects at energies around 185 eV for a pair and 35 keV for a cluster, respectively.[7] The increase in energy to create a cluster is due to the need to collide with a recoil atom to displace additional atoms. While ionization damages will repair naturally, the concentrated cluster of defects will lead to the creation of electrically active sites. If these have deep energy levels within the bandgap, they can cause charge recombination sites and can result in reverse current and a loss in performance.[8,9] To mitigate this damage, shielding is placed around the devices. This shielding is mainly in the form of cerium doped glass or fused silica sheets for outside electronics such as solar cells, and polyethylene radiation shielding for inside systems, due to the hydrogen-rich molecules.[10–12] An example of the damage caused by radiation-induced defects can be seen in the radiation hardness of triple-junction solar cells such as InGaP/InGaAs/

Ge. While they are the most prominent solar technology used in space, due to their high efficiency, they are exceedingly sensitive to radiation and have been shown to undergo an 80% drop in PCE performance after irradiation with 150 keV protons at a fluence of 1×10^{11} protons cm^{-2} and with 1 MeV protons at a fluence of 1×10^{13} protons cm^{-2}.[13–15] Moving attention to the radiation hardness of perovskite solar cells (PSCs), and while it is still an active field of investigation, in comparison to other technologies it is one that is in its infancy. Despite this, a few notable publications are investigating a wide range of energies, device architectures, perovskite compositions, and materials.[16–29] In 2015, and once again in 2018, Miyasaka et al. showed that PSCs provide a much more robust radiation stable solar cell than their inorganic counterparts. In these publications, it was reported that PSCs utilizing a compact and mesoporous TiO$_2$ electron transport layer (ETL) and P3HT hole transport layer (HTL) are stable under an accumulated dose of 1×10^{14} protons cm^{-2} for 50 keV protons and 1×10^{16} electrons cm^{-2} for 1 MeV electrons.[17,18] In 2019, Barbé et al. looked at the radiation stability of perovskite devices with aluminum-doped zinc oxide (AZO) as the TCO and Spiro-OMeTAD as the HTL.[16] The devices were bombarded with 150 keV protons and were stable up to a fluence of 1×10^{13} protons cm^{-2}. However, at higher fluences, specifically 1×10^{15} protons cm^{-2}, the devices were completely degraded. This sharp decline in performance was attributed to the degradation of the HTL, resulting in an increase in interfacial recombination.[16] More recently (2021), two groups have looked at low energy proton stability of perovskite devices, with both groups tested with a proton energy of 50 keV. Durant et al. show that under the bombardment of 50 keV protons, degradation is not observed until a fluence of 1×10^{12} protons cm^{-2} and is mostly the result of decreased V_{oc} rather than J_{sc}. Additionally, increased proton energy results in a shift from nuclear collisions to electronic ionizing energy loss within the perovskite layer, which leads to a 20% improvement in V_{oc} and maximum power output under AM0 illumination.[27] In contrast, Zhao et al. showed a new vacancy-ordered double perovskite (Cs$_2$CrI$_6$) that exhibits excellent device performance and irradiation resistance under 50 keV protons. The devices retain 90% of initial PCE under a proton fluence of 5×10^{13} protons cm^{-2}, which indicates a promising potential for application in photovoltaic cells and α-particle detectors for space applications.[28]

In this work, we present a detailed study on the effect of 150 keV protons on the performance of an all-screen printed, HTL free, carbon electrode perovskite solar cells. Owing to the low cost, easy processing, and scalability, screen-printed carbon electrode PSCs have revolutionized the techniques used to manufacture PSCs.[30–32] This is due to the ability to fully print each layer, with mesoporous materials, and then to infiltrate the entire stack with perovskite. Alongside being easier to manufacture than traditional PSCs, carbon-based devices have been shown as more stable than other architectures. They boast superior lifetimes under UV and continuous illumination, alongside exhibiting robust thermal and moisture stability due to the removal of the HTL and the thick carbon electrode acting as efficient encapsulation.[33–35] The devices were exposed to 150 keV proton irradiations from 1×10^{12} to 1×10^{15} protons cm^{-2}. We demonstrate that the cells can withstand proton irradiation up to 1×10^{15} protons cm^{-2} without loss in efficiency. This corresponds to ≈1000 years in an LEO.[30] The structural and optical properties of individual layers in the device stack were probed through Raman and photoluminescence spectroscopy/mapping, respectively. Simulation was applied to compare the proton stopping power for mesoporous carbon against common metal contacts such as gold (Au), silver (Ag), aluminum (Al), and copper (Cu) at 150 keV proton energy.

2. Results and Discussion

The device architecture is shown in **Figure 1**a and is a glass/FTO/TiO$_2$/ZrO$_2$/carbon mesoporous stack, infiltrated with CH$_3$NH$_3$PbI$_3$-AVA (MAPI-AVA). The current–voltage (J–V) curves under AM1.5G and AM0 illumination for the champion cell are shown in Figure 1b. Due to the small range of PCEs obtained, two samples were chosen for each fluence. Figure 1b also shows the device parameters for the champion cells under 1 sun AM1.5G and 1 sun AM0 illumination, respectively. Figure S1a, Supporting Information, shows the histogram of the 1 sun AM1.5G device efficiencies before proton irradiation. The performances of cells under 1 sun AM1.5G illumination vary between 11% and 13% with an active area of 1 cm^2 and mask size of 0.49 cm^2, which for this architecture is reasonable. For reference, a histogram of the PCE under 1 sun AM0
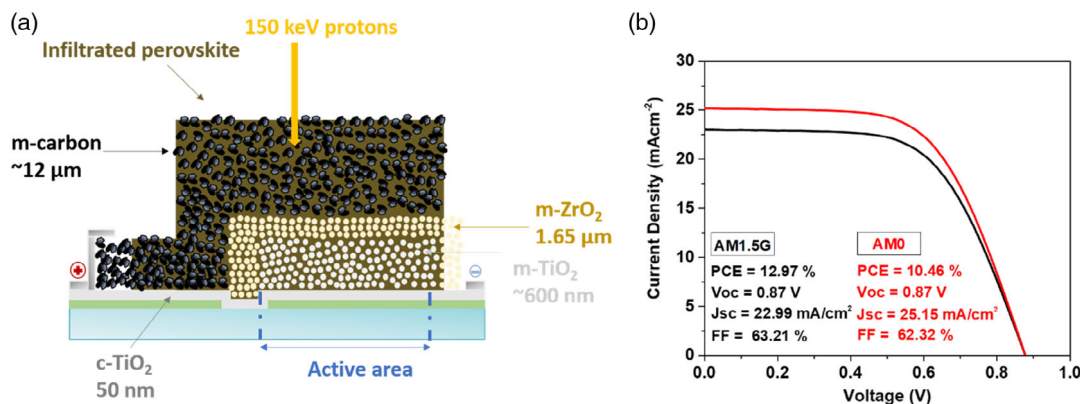

Figure 1. a) Device architecture of the mesoporous-carbon-based perovskite solar cells (m-CPSC). Arrow shows the direction of incident protons. b) J–V curves under 1 sun AM1.5G and 1 sun AM0 illumination for the champion cell.

illumination before bombardment is shown in Figure S1b, Supporting Information. The lower PCE compared to other device architectures is mainly due to the high series resistance (R_S) of the carbon electrode. The lower PCE here compared with the best PCE mesoporous carbon-based peroksite solar cells (m-CPSCs) reported (use the same infiltration method and device layers) is mainly due to the larger active area and large mask size used. Here, a relatively large active area was fabricated with a relatively large mask for the testing, which is more appropriate to test its scalability "Tong et al." present an excellent investigation into the effect of mask size on m-CPSC performance.[36] They show that around the mask size used here, there is a decrease in fill factor (FF) and PCE. As a reference, the current record PCE of mesoporous carbon electrode cells is 17.02%, however, compared to our work, their devices utilize a NiO HTL and they used a two-step deposition method to infiltrate a triple cation perovskite.[37] From here onward, we will concentrate on the AM0 performance as this is more appropriate when considering the aerospace applications of these m-CPSCs. At 1 sun AM0, the champion cell has PCE > 10%, and the J_{sc} is higher than that at 1 sun AM1.5G, as the light intensity of 1 sun AM0 is about 1.36 times higher than that at 1 sun AM1.5G (while the V_{OC} and FF are similar to that under 1 sun AM1.5G).

To probe the stability of the carbon electrode itself and its encapsulation potential, we bombarded all samples through the carbon electrode with 150 keV protons with fluences ranging from 1×10^{12} to 1×10^{15} protons cm^{-2}. Some devices were not exposed to proton irradiation but subjected to the same atmospheric conditions to serve as control samples. All samples were kept under N$_2$ in the dark before irradiation was carried out, and then kept for a week under dark air after bombardment, before they were returned from the Surrey Ion Beam Centre and remeasured. The changes in PV parameters (PCE, V_{oc}, J_{sc}, and FF) after proton irradiation are shown in **Figure 2**a. Here, we show the remaining factors for the different fluences under

1 sun AM0 illumination. The remaining factor was calculated by taking the ratio of the PV parameters before and after irradiation, for each fluence. These were then normalized with respect to the control samples. Interestingly, the PCE, V_{oc}, J_{sc}, and FF all remained close to a remaining factor of 1.0 and sometimes even being slightly higher, as seen at 1×10^{15} protons cm^{-2}. Due to the parameters remaining consistent, even at 1×10^{15} protons cm^{-2}, it is suggested that the devices were not degraded. The remaining factors were also measured under 1 sun AM1.5G illumination and are shown in Figure S2, Supporting Information, indicating a similar trend as under 1 sun AM0 illumination. Additionally, the full AM0 PV parameter values before and after bombardment are shown in Table S1, Supporting Information.

The external quantum efficiency (EQE) for representative cells at each proton fluence is shown in Figure 2b. The EQE of the devices are quite similar without a trend with increasing proton fluence, therefore in fair agreement with the stable J_{sc} obtained from current density–voltage measurements (Figure 2a). In other works looking at comparable irradiation conditions, Miyasaka et al. showed that a non-uniform spectral response of photocurrent in FAMAPb(IBr)$_3$ cells after proton irradiation at a fluence of 1×10^{14} protons cm^{-2} is attributed to the degradation of the active layer.[17] This can be circumvented using more stable perovskite compositions, as used herein.[19,23] Barbé et al. showed that a uniform reduction in the EQE spectrum was indicative of a deterioration in charge extraction properties rather than charge generation properties suggesting a degradation of the Spiro-OMeTAD HTL properties.[16] Here, we see no significant change in EQE across the proton fluences. Therefore, we infer that there is no degradation of the active layer or a change in charge extraction properties of the mesoporous carbon electrode as a result of the proton bombardment. However, we do note that the EQE values do not necessarily match the measured J_{sc}. This is due to the mesoporous nature of the active area and the monochromatic beam focus used for the EQE measurements being smaller than the probing area for
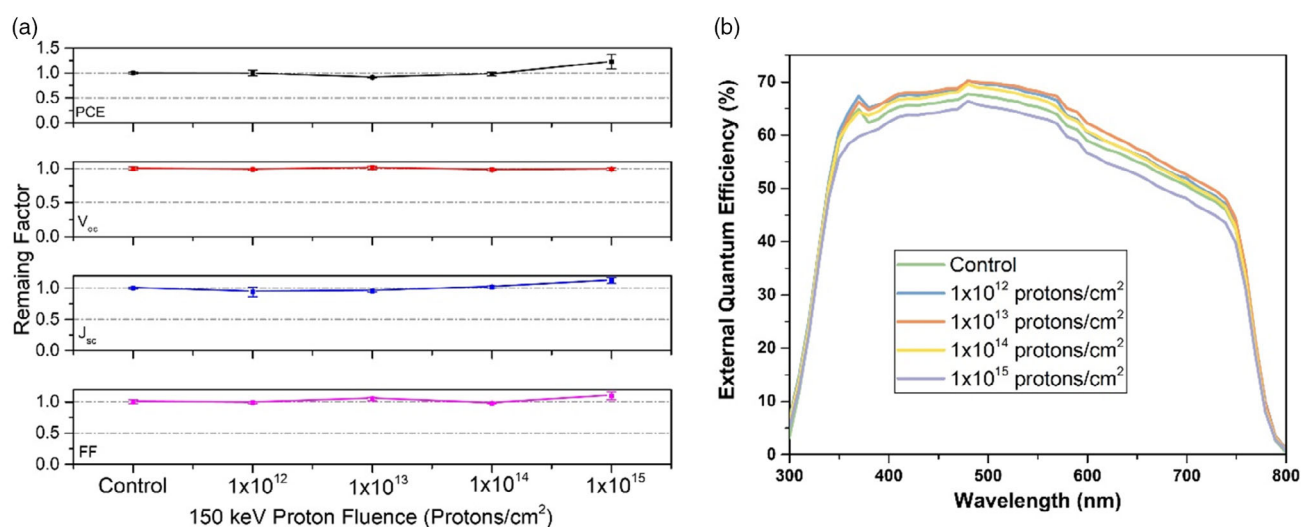

Figure 2. a) Remaining factor of PCE, V_{oc}, J_{sc}, and FF (under 1 sun AM0 illumination) versus proton fluence of m-CPSC (including the control device). The data points are the average values at each fluence and the error bars represent the range of values. b) The EQE for the devices after the 150 keV proton bombardment.

J_{sc}. While we used quite a standard way to measure the EQE, it would be nice to consider future improvement in EQE measurement for this highly mesoscopic type of perovskite solar cells. For example, a raster scan over the active area should lead to a better average EQE.

Therefore, from these measurements, it is shown that screen-printed PSCs utilizing a mesoporous carbon electrode can be exposed to a radiation level up to 1×10^{15} protons cm^{-2} at 150 keV, without being significantly degraded. By comparison, the V_{oc} and J_{sc} of Si solar cells exposed to 150 keV protons decreased by >40% and 10%, respectively, at 1×10^{13} protons cm^{-2}.[14] At this same proton energy, GaAs solar cells exhibit a ≈40% decrease in PCE at a fluence of 1×10^{11} protons cm^{-2}.[15] In addition, planar PSCs fabricated with an Au electrode and Spiro-OMeTAD HTL, are stable up to 1×10^{13} protons cm^{-2} when exposed to 150 keV protons, and at 1×10^{15} protons cm^{-2} are completely degraded due to interfacial recombination at the perovskite/HTL interface.[16] Furthermore, 100 keV proton bombardment on flexible inverted PSCs show an initial ≈20% performance decrease at 1×10^{13} protons cm^{-2} due to a reduction in the FF, but this decrease is recoverable.[23] Therefore, at this proton energy range, screen-printed carbon PSCs exhibit the greatest stability and present a much more robust and stable platform for solar cells for space applications.

Next, we used non-destructive techniques to investigate why these PSCs remain stable under the proton bombardment and subsequently gain a better understanding of the radiation hardness of the mesoporous carbon layer. We used micro-Raman mapping also to study the homogeneity of the device layers. The normalized averaged Raman spectra taken from the glass side, for each fluence and control, is shown in **Figure 3**a which shows three important peaks. The first peak is a wide peak at ≈100 cm^{-1}, which is associated with the vibrational modes of the methyl ammonia (MA) cations of MAPI.[38] The second peak is at 145 cm^{-1}, which is the signal from the anatase phase of the TiO$_2$ ETL used in the devices, and the third peak at 245 cm^{-1} is related to a MA vibrational mode. As the Raman intensity can be sensitive to measurement conditions, such as focussing

(particularly for the mesoporous structure), it should be more accurate to normalize the Raman spectra (normalized to the peak at 145 cm^{-1}). The Raman spectra before the normalization are shown in Figure S3a, Supporting Information. The broader perovskite peak, at 100 cm^{-1}, is more prevalent in the normalized data. The spectra at 145 cm^{-1} overlap each other perfectly, consistent with no degradation in the TiO$_2$ chemical structure. There is also no considerable change for the peaks at 100 and 245 cm^{-1}, consistent with no degradation on the perovskite structure.

Next, micro-photoluminescence (PL) mapping of the full device stack before and after proton irradiation was also measured, to further look at the stability (regarding optical properties) and device homogeneity. As these devices are unencapsulated, the use of Raman and PL can be useful to probe not only the effects of the proton bombardment of the cells but also the effect of storage and transport as these cells were under air for around 2 weeks during the experimental time and travel time before were remeasured. To investigate the effect of PL on the mesoporous structure (inhomogeneous structure), it should be again more accurate to study the normalized PL data with the proton fluences. As shown in Figure 3b, there are no PL peak shifts from the perovskite (773 nm) with excellent PL spectral overlap among the proton fluences. This finding is consistent with no considerable degradation of the PL properties and indicates that there is no phase separation in the perovskite as observed for mixed FAMAPb(Br)$_3$-based devices.[18] For reference, the PL spectra before the normalization are shown in Figure S3b, Supporting Information, and the PL mapping after the proton bombardments are shown in Figure S4, Supporting Information (which shows that there is large inhomogeneity in the PL intensity at 773 nm within the individual maps for each proton fluence). In addition, these significant variations do not change with proton fluence and are present even in the control device. The significantly non-uniform PL intensity across the same device could be explained by the mesoporous nature of the layers. Therefore, even considering the exposure to ambient air, the Raman data and PL data above are consistent with no significant degradation
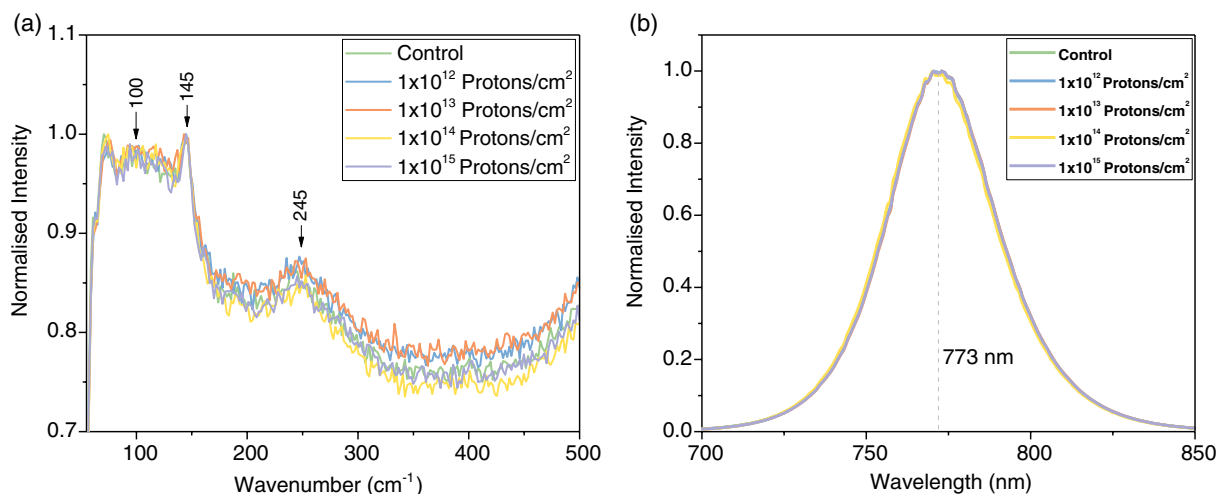

Figure 3. a) Normalized Raman spectra of perovskite solar cells measured between 50 and 500 cm^{-1} and b) normalized PL spectra of perovskite solar cells, as a function of proton fluence through the glass substrate.
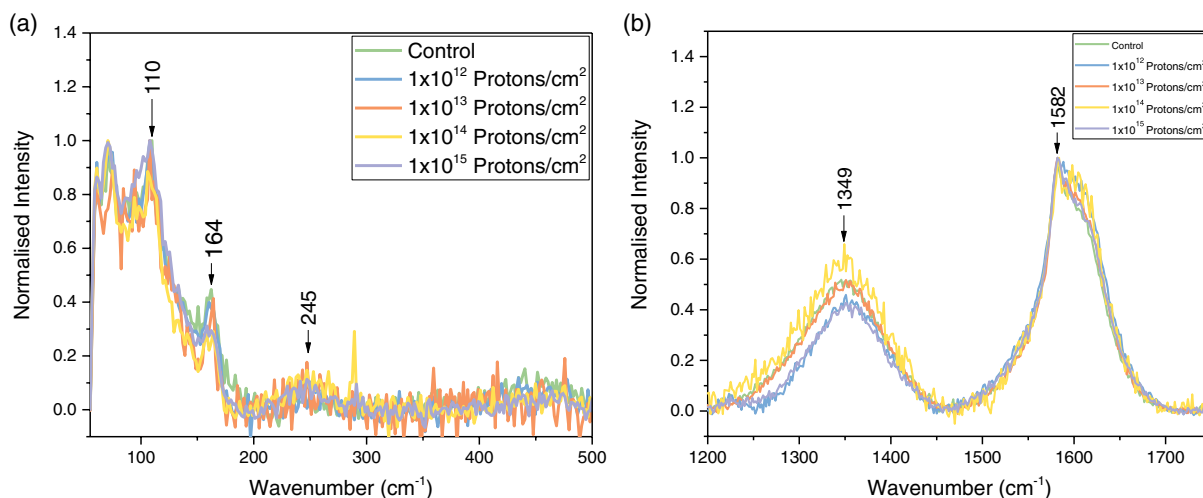
Figure 4. Normalized Raman spectra of perovskite solar cells measured between a) 50 and 500 cm^{-1} and b) 1200 and 1750 cm^{-1} as a function of proton fluence through the carbon electrode.

structurally and optically, agree well with no considerable degradation of the PCE of the m-CPSCs.

While PL and Raman spectroscopy/mapping were applied on the glass substrate side of the devices to investigate the perovskite embedded in mesoporous TiO$_2$, that is, the active area of the cell, the same techniques were also applied to the carbon electrode. Here, illumination was applied to the mesoporous carbon electrode to probe structural and optical changes in the perovskite embedded within the mesoporous carbon layer, near the surface ($\approx 2\,\mu$m).[39] Due to the rough carbon face, here we focus on discussing the normalized Raman data which is shown in **Figure 4**. The PL spectra of perovskite from the carbon electrode showed random peak shift (data not shown), it is not discussed further here as it is not well understood.

Figure 4a shows the perovskite Raman signal, while Figure 4b shows the Raman signal from the mesoporous carbon electrode, after the proton irradiation. In comparison to the Raman measurements taken from the glass side, the overall perovskite Raman signal is weaker due to the increase in light scattering from the carbon electrode. Therefore, it is particularly better to focus on the normalized Raman data, however, the raw data is also provided in Figure S5a, Supporting Information, for reference. In Figure 4a, there are three main Raman peaks. The first peak is at 110 cm^{-1}, the second peak at 164 cm^{-1}, and the third peak at 245 cm^{-1}. The plot has been normalized to the peak at 110 cm^{-1}, which along with the peak at 164 cm^{-1}, had been attributed to the formation of dihydrated MAPI,[40] in which both peaks have been shown to be more prominent with increasing humidity level. The broad peak at 245 cm^{-1} is again attributed to MA cation torsional modes.[41] For each of the three peaks, however, there is no clear trend between the relative peak intensity with the proton fluence. This suggests that the amount of moisture present, and therefore di-hydrated MAPI, in each device is random. However, even with the measured presence of di-hydrated perovskite in the carbon devices electrode (and the PL peak shift), the PV performance remains similar between the devices. This could be explained by the fact that the Raman data (and PL data) collected are mainly from the "capping" layer

of perovskite/m-carbon which is not involved in device functionality. These results also show the apparent stability of the m-CPSCs during storage and transportation.

Figure 4b shows the normalized Raman intensity from the range 1200–1750 cm^{-1}, where there are two clear peaks at 1349 and 1582 cm^{-1}, which can be assigned to the D and G bands of carbon, respectively (for reference, the raw data is also provided in Figure S5b, Supporting Information). The D peak is only visible in sp^2 hybridized carbon systems and arises due to the defects in the layer. The more defects that are present in the carbon layer, the higher the intensity of the D-band relative to the G-band.[42,43] The G peak is due to stretching of the C—C bond in graphitic materials which can be used to investigate any modification to the structure, and is common to all sp^2 carbon systems. In Figure 4b, which has been normalized to the G-band, there is a very good overlap at the 1582 cm^{-1} peak. This overlap suggests that even with the proton bombardment (and the presence of moisture), there is no considerable change in the structure of the carbon. However, there are some variations in D-band intensity with no discernible trend with proton fluence. It has been shown that an increase in disorder can be observed as a result of ion bombardment, but using much lower ion energy (normally in the eV range).[44] Here, we suggest that due to the mesoporous nature of the carbon, the disorder within the layer can be random among the devices, as the carbon domain size, and therefore roughness can be inhomogenous between each device. For reference, the Raman mapping for the D-band is shown in Figure S6, Supporting Information, which shows significant inhomogeneity of the D-band intensity even within the same device. This variation is likely due to the mesoporous nature of the carbon layer.

To understand why the perovskite in the meso-carbon devices exhibits superior proton bombardment stability against other device structures using metal electrodes, simulations were performed to compare the proton stopping power of the carbon electrode and other metal alternatives. This simulation should provide a better understanding of the penetration depth of the proton beam, and subsequently the layers most affected by
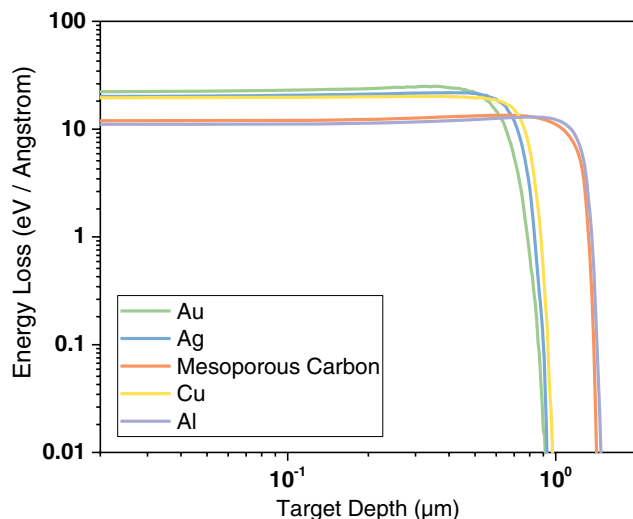
**ADVANCED
SCIENCE NEWS**
www.advancedsciencenews.com

Energy Technology
Generation, Conversion, Storage, Distribution
www.entechnol.de

Figure 5. Log–log plot of 150 keV proton energy loss in the electrodes as a function of electrode thickness (target depth).

the proton implantation. The simulation package used was The stopping and range of ions in matter and its sister programme, transport of ions in matter. This package was used to calculate the lower proton energy (150 keV) stopping range.

Figure 5 shows the energy loss at 150 keV, as a function of target depth, for the electrode materials. Here, target depth is the thickness of the (electrode) materials. From this plot, gold and silver possess the shortest stopping range with 150 keV protons, with protons completely stopped at a target depth of ≈900 nm and therefore can be regarded as the best metal electrode for stopping 150 keV protons from those investigated here. This is followed by copper, mesoporous carbon, and aluminum. For mesoporous carbon, protons stop at a target depth of 1.27 μm Although meso-carbon has lower proton stopping power than most of the electrodes, the thickness of the meso-carbon used in the devices is ≈12 μm, which is significantly thicker than the thickness required to stop the protons. This finding is consistent with the superior proton stability of the devices with 150 keV proton even at 1×10^{15} protons cm^{-2}. The perovskite embedded in the mesoporous TiO$_2$ layer (which is the PV active region), more than 12 μm away from the mesoporous carbon surface, is therefore actually shielded from the 150 keV protons by the thick carbon electrode. Therefore, the performance of the cells are unchanged after irradiation even up to a fluence of 1×10^{15} protons cm^{-2}. In contrast, the perovskite close to the carbon surface (not within the PV active region) is not shielded, however, even though degradation due to protons (and moisture) can occur at this region, it has no effect on the device parameters.

The interesting and the most notable result from these simulations is that the mechanisms that lead to good device performance also play a crucial role in proton radiation stability. For effective electrode conductivity in the m-CPSC architecture, the carbon layer is required to be thick (≈12 μm), and from the simulations, this required thickness is far greater than that needed to stop the incident protons. Therefore, the device design already incorporates impressive proton radiation shielding. In contrast,

for other common metal electrodes simulated here, the required thickness of the metal to stop the 150 keV protons is about one order of magnitude thicker than their normal thickness (100 nm) used for perovskite solar cells. Our simulation shows that a significant increase in the metal thickness could stop the 150 keV protons, but it could be challenging and expensive to achieve that thickness using the thermal evaporation approach.

3. Conclusion

The screen-printed perovskite solar cells with a mesoporous carbon electrode have a very high tolerance to 150 keV proton irradiation, even up to a proton fluence of 1×10^{15} protons cm^{-2}. In comparison, PSCs with a gold electrode in standard device architecture are only stable up to 1×10^{13} protons cm^{-2}. Photoluminescence and Raman spectroscopy/mapping measured from the glass side is consistent with no phase separation of the perovskite and no considerable degradation of the perovskite embedded in the mesoporous TiO$_2$ layer (as well as the TiO$_2$ layer). Raman peaks at 110 and 164 cm^{-1} observed when probed from the carbon side are consistent with the presence of dihydrated MAPI (indicating the presence of some moisture), which would have originated from the storage and transport between measurements and bombardment. Importantly, this does not affect the device performance, as the degraded region is not within the PV active area. Furthermore, the G-band of the carbon electrode remains unchanged, suggesting no considerable change in the electrode chemical structure upon the proton irradiation. Our simulation shows that the origin of the superior proton stability is inherently due to the high thickness of the carbon electrode rather than the proton stopping power of the material itself. This finding coupled with its reported good UV/photostability and thermal stability, along with cheaper manufacturing costs compared to conventional metal electrodes, shows that PSCs with a carbon electrode, mesoporous or planar, could have the attractive potential for space applications.

4. Experimental Section

Device Fabrication: Carbon cell preparation: The FTO substrate was initially patterned with an Nb:YVO$_4$ laser (532 nm), then cleaned with a solution of Hellmanex (2%, deionized water), rinsed with acetone, IPA, and finally plasma cleaned in an O$_2$ atmosphere for 5 min. A compact TiO$_2$ blocking layer was sprayed with a solution of 10% titanium di-isopropoxide bis (acetylacetonate) (TAA, 75% in IPA, Sigma–Aldrich) on the FTO substrate, which was kept at 300 °C on a hot plate. After the deposition of C-TiO$_2$, the mesoporous TiO$_2$ paste was diluted 1:1 by weight in terpineol (95%, Sigma-Aldrich), screen-printed, and sintered at 550 °C. Next, the mesoporous ZrO$_2$ (Solaronix) and carbon paste (Gwent electronic materials) were sequentially screen-printed and each annealed at 400 °C. Perovskite precursor solution (0.439 g PbI$_2$ (99%, Sigma–Aldrich), 0.1514 g MAI (CH$_3$NH$_3$I, anhydrous, Dyesol), and 0.0067 g 5-ammonium valeric acid iodide (5-AVAI, Dyesol) in 1 ml γ-butyrolactone (Sigma–Aldrich)) then dropped cast (15 μl) onto the cooled stack. Devices were left in the air for 10 min to allow the solution to percolate through the stack, before annealing in an oven for 1 h at 50 °C. The finished cells were then exposed to a standard 70% relative humidity process at 40 °C for 24 h to induce a recrystallization and then dried under vacuum before measuring.

J–V Characterization: The J–V characteristics of the perovskite devices were recorded with a digital source meter (Keithley model 2400, USA) and

450 W xenon lamp (Sol3A Class AAA Solar Simulator, Oriel, USA). The light source was equipped with an Air Mass filter (Newport) to correct the output of the xenon lamp to better match the AM1.5G solar spectrum. Both forward and reverse bias scans were taken from 1.2 to −0.1 V with a sweep interval of 0.015 V and a light soaking delay time of 3 min between each scan. The Air Mass 0 J–V characteristics follow the same experimental set-up and measurement parameters as AM1.5G. However, the AM1.5G filter was replaced with an AM0 filter. Alongside this replacement, the lamp was calibrated by measuring a GaAs calibration cell, and matching the measured J_{SC} value with the quoted GaAs device J_{sc} value under the AM0 spectrum.

Proton Bombardment: The proton beam irradiation was carried out at the Surrey Ion Beam Centre in the UK. The reference samples have traveled together with the irradiated samples. All the samples were packed in an N_2 atmosphere in the dark during traveling. The reference samples (not irradiated) were exposed to air when the other samples were also exposed to air just before the proton irradiation and during the travel back to Swansea. Sample loading was carried out in a class 100 clean room. The perovskite cells were mounted directly onto 4 in. support plates which were inserted into a carousel wheel in the sample chamber. Silver paste was applied to allow charges to be conducted to the back of the samples and in the holder plate to avoid charges accumulation. Samples were loaded in a 7°/0° tilt/twist orientation to the incident beam and implanted under vacuum ($2.3 \pm 0.2 \times 10^{-6}$ mbar). The samples were placed to receive direct impact of the protons, with the back contact (carbon electrode) facing the proton source. A Danfysik 1090 low energy high current implanter was used to implant 150 keV protons into the samples (from the mesoporous carbon side). The fluence rate was controlled to 3×10^{10} cm^{-2} s for fluence 10^{12} protons cm^{-2} and 3×10^{11} cm^{-2} s for fluences 10^{13} to 10^{15} protons cm^{-2}.

EQE Measurements: EQE measurements were made using a monochromatic light source in AC mode with a chopping frequency of 70 Hz (QEX10 PV Measurements). The system was calibrated using a NIST-certified calibration cell (PV Measurements) and data points were taken by sweeping the wavelength from 300 to 800 nm and recording a value every 10 nm. There was also a 30 s delay between grating changes due to the slow response time of the devices.

Raman and PL Characterization: The Raman and PL measurements were performed with a Renishaw inVia Raman system (Renishaw plc., Wotton-Under-Edge, UK) in a backscattering configuration. A 532 nm laser and 50× objective were used (NA: 0.50, spot size ≈ 1 μm). For the Raman measurements, a laser power of 150 μW and acquisition time of 10 s were used to measure a map of 25 different points, which were averaged in a single spectrum. For the PL measurements, a laser power of 300 nW and an acquisition time of 2 s were used to measure a map of 121 different points, which were also averaged to obtain a single spectrum.

Supporting Information

Supporting Information is available from the Wiley Online Library or from the author.

Conflict of Interest

The authors declare no conflict of interest.

Data Availability Statement

Research data are not shared.

[1] R. W. Fillius, *J. Geophys. Res.* **1966**, *71*, 97.
[2] S. Freden, *Space Sci. Rev.* **1969**, *9*, 198.
[3] M. S. L. Maria, *Master of Science in Engineering Physics Thesis, Embry-Riddle Aeronautical University, Daytona Beach, Florida*, **2011**.
[4] J. R. Srour, J. W. Palko, *IEEE Trans. Nucl. Sci.* **2013**, *60*, 1740.
[5] R. Smith, D. E. Harrison, B. J. Garrison, *Phys. Rev. B* **1989**, *40*, 93.
[6] V. S. Vavilov, *Effects of Radiation on Semiconductors*, Consultants Bureau, New York **1967**.
[7] M. Stefano, *Radiation Damage for Silicon Wafers*, CERN, Geneva, **2018**.
[8] M. Moll, *Doctor of Philosophy in Physics Thesis, University of Hamburg*, **1999**.
[9] V. V. Emtsev, T. V. Mashovets, V. V. Mikhnovich, N. A. Vitovskii, *Radiat. Effects Defects Solids* **1989**, *111–112*, 99.
[10] D. F. Medina, *Handbook of Cosmic Hazards and Planetary Defence*, Springer, Cham, **2015**, p. 295.
[11] C. A. Carosella, *J. Spacecraft Rockets* **1968**, *5*, 878.
[12] L. Narici, M. Casolino, L. D. Fino, M. Larosa, P. Picozza, A. Rizzo, V. Zaconte, *Sci. Rep.* **2017**, *7*, 1644.
[13] T. Ohshima, S. I. Sato, T. Nakamura, M. Imaizumi, T. Sugaya, K. Matsubara, S. Niki, A. Takeda, Y. Okano, in *Conf. Rec. IEEE 39th Photovolt. Spec. Conf.*, IEEE, Tampa **2013**, p. 2779.
[14] R. M. Burgess, W. S. Chen, W. E. Devaney, D. H. Doyle, N. P. Kim, B. J. Stanbery, in *IEEE 20th Photovolt. Spec. Conf.*, Vol. 2, IEEE, New York **1988**, p. 909.
[15] R. Loo, S. Kamath, R. C. Knechtli, *Low Energy Proton Radiation Damage to (AlGa)As-GaAs Solar Cells*, NASA, Malibu, **2013**.
[16] J. Barbé, D. Hughes, Z. Wei, A. Pockett, H. K. H. Lee, K. C. Heasman, M. J. Carnie, T. M. Watson, W. C. Tsoi, *Solar RRL* **2019**, *3*, 1900219.
[17] Y. Miyazawa, M. Ikegami, T. Miyasaka, T. Ohshima, M. Imaizumi, K. Hirose, in *2015 IEEE 42nd Photovoltaic Specialist Conf. (PVSC)*, IEEE, Piscataway, NJ **2015**.
[18] Y. Miyazawa, M. Ikegami, H.-W. Chen, T. Ohshima, M. Imaizumi, K. Hirose, T. Miyasaka, *iScience* **2018**, *2*, 148
[19] F. Lang, O. Shargaieva, V. V. Brus, H. C. Neitzert, J. Rappich, N. H. Nickel, *Adv. Mater.* **2017**, *30*, 1702905
[20] F. Lang, M. Jošt, J. Bundesmann, A. Denker, S. Albrecht, G. Landi, H.-C. Neitzert, J. Rappich, N. H. Nickel, *Energy Environ. Sci.* **2019**, *12*, 1634.
[21] J. S. Huang, M. D. Kelzenberg, P. Espinet-Gonzalez, C. Mann, D. Walker, A. Naqvi, N. Vaidya, E. Warmann, H. A. Atwater, *iScience*, **2018**, 1248.
[22] K. Yang, K. Huang, X. Li, S. Zheng, P. Hou, J. Wang, H. Guo, H. Song, B. Li, H. Li, B. Liu, X. Zhong, J. Yang, *Org. Electron. Phys. Mater. Appl.* **2019**, *71*, 79.

[23] O. Malinkiewicz, M. Imaizumi, S. B. Sapkota, T. Ohshima, S. Öz, *Emergent Mater.* **2020**, *3*, 9.

[24] N. H. Nickel, F. Lang, V. V. Brus, J. Bundesmann, S. Seidel, A. Denker, S. Albrecht, G. Landi, H. C. Neitzert, *Physics, Simulation, and Photonic Engineering of Photovoltaic Devices VII*, SPIE, **2018**, 10527.

[25] F. Lang, N. H. Nickel, J. Bundesmann, S. Seidel, A. Denker, S. Albrecht, V. V. Brus, J. Rappich, B. Rech, G. Landi, H. C. Neitzert. *Adv. Mater.* **2016**, *28*, 39.

[26] D. Pérez-del-Rey, C. Dreessen, A. M. Igual-Muñoz, L. van den Hengel, M. C. Gélvez-Rueda, T. J. Savenije, F. C. Grozema, C. Zimmermann, H. J. Bolink, *Solar RRL* **2020**, *7*, 12.

[27] B. K. Durant, H. Afshari, S. Singh, B. Rout, G. E. Eperon, I. R. Sellers, *ACS Energy Letters* **2021**, *6*, 2362.

[28] P. Zhao, J. Su, Y. Guo, L. Wang, Z. Lin, J. Zhang, Y. Hao, X. Ouyang, J. Chang, *Mater. Today Phys.* **2021**, *20*, 100446.

[29] F. Lang, M. Jošt, K. Frohna, E. Köhnen, A. Al-Ashouri, A. R. Bowman, T. Bertram, A. B. Morales-Vilches, D. Koushik, E. M. Tennyson, K. Galkowski, G. Landi, M. Creatore, B. Stannowski, C. A. Kaufmann, J. Bundesmann, J. Rappich, B. Rech, A. Denker, S. Albrecht, H. C. Neitzert, N. H. Nickel, S. D. Stranks, *Joule* **2020**, *4*, 5.

[30] J. Baker, K. Hooper, S. Meroni, A. Pockett, J. Mcgettrick, Z. Wei, R. Escalante, G. Oskam, M. Carnie, T. Watson, *J. Mater. Chem. A* **2017**, *5*, 18643.

[31] S. M. P. Meroni, Y. Mouhamad, F. De Rossi, A. Pockett, J. Baker, R. Escalante, J. Searle, M. J. Carnie, E. Jewell, G. Oskam, T. M. Watson, *Sci. Technol. Adv. Mater.* **2018**, *19*, 1.

[32] C. Zhou, S. Lin, *Solar RRL* **2019**, *4*, 1900190.

[33] V. Babu, R. F. Pineda, T. Ahmad, A. O. Alvarez, L. A. Castriotta, A. D. Carlo, F. Fabregat-Santiago, K. Wojciechowski, *ACS Appl. Energy Mater.* **2020**, *3*, 5126.

[34] S. G. Hashmi, A. Tilihonen, D. Martineau, M. Ozkan, P. Vivo, K. Kaunisto, V. Ulla, A. M. Zakeeruddin, M. Grätzel, *J. Mater. Chem. A* **2017**, *5*, 4797.

[35] O. Malinkiewicz, M. Imaizumi, S. B. Sapkota, T. Ohshima, S. Öz, *Emergent Mater.* **2020**, *3*, 9.

[36] C. Tong, W. Ji, D. Li, A. Mei, Y. Hu, Y. Rong, H. Han, *J. Mater. Chem. A* **2019**, *7*, 10942.

[37] S. M. P. Meroni, C. Worsley, D. Raptis, T. M. Watson, *Energies* **2021**, *14*, 386.

[38] M. A. Pérez-Osorio, Q. Lin, R. T. Phillips, R. L. Milot, L. M. Herz, M. B. Johnston, F. Giustino, *J. Phys. Chem. C* **2018**, *122*, 21703.

[39] K. E. A. Hooper, H. K. H. Lee, M. J. Newman, S. M. P. Meroni, J. Baker, T. M. Watson, W. C. Tsoi, *Phys. Chem. Chem. Phys.* **2017**, *19*, 5246.

[40] H. Lakhiani, T. Dunlop, F. De Rossi, S. Dimitrov, R. Kerremans, C. Charbonneau, T. Watson, J. Barbé, W. C. Tsoi, *Adv. Funct. Mater.* **2019**, *29*, 1900885.

[41] P. Ahlberg, F. O. Johansson, Z. B. Zhang, U. Jansson, S. L. Zhang, A. Lindblad, T. Nyberg, *APL Mater.* **2016**, *4*, 046104.

[42] P. Pistor, A. Ruiz, A. Cabot, V. Izquierdo-Roca, *Sci. Rep.* **2016**, *6*, 35973.

[43] A. C. Ferrari, J. Robertson, *Philos. Trans. R. Soc. Lond. Ser. A: Math. Phys. Eng. Sci.* **2004**, *362*, 2477.

[44] L. Bokobza, J. L. Bruneel, M. Couzi, *C J. Carbon Res.* **2015**, *1*, 77.

2100928 (8 of 8)